Journal of Materials Chemistry A

PAPER

View Article Online
View Journal | View Issue

Cite this: J. Mater. Chem. A, 2017, 5, 24720

Investigation of chloride ion adsorption onto Ti_2C MXene monolayers by first-principles calculations†

Dashuai Wang,[a] Yu Gao,[a] Yanhui Liu,[c] Yury Gogotsi,*[ab] Xing Meng,[ab] Gang Chen*[a] and Yingjin Wei*[a]

Received 15th October 2017
Accepted 5th November 2017

DOI: 10.1039/c7ta09057a

rsc.li/materials-a

Chloride ion adsorption on Ti_2C monolayers was theoretically investigated. Electrochemical parameters, including specific capacity, chloride ion (Cl^-) diffusion barrier, and discharge voltage profile, were studied *via* first-principles calculations. The most favorable Cl^- adsorption configuration was identified using a partial particle swarm optimization algorithm and the results showed that Cl^- adsorption onto Ti_2C monolayers achieved a large theoretical capacity (331 mA h g^{-1}), high working voltage (4.0–3.5 V), and low diffusion barrier (0.22 eV). This resulted in excellent rate capability and a large specific energy of 1269 W h kg^{-1} at the material level. The effects of terminal O, F, and OH groups on Cl^- adsorption onto Ti_2C monolayer were also studied, which showed that Cl^- could not be adsorbed onto O and F terminated Ti_2C monolayers. In comparison, Cl^- adsorption onto OH terminated Ti_2C was allowed but generated a smaller specific capacity (126 mA h g^{-1}) and lower working voltage (3.5–1.5 V) than a bare Ti_2C monolayer.

1. Introduction

Lithium ion batteries (LIBs) have been an essential technology in our daily life from portable electronics to electric vehicles and the smart grid. But, highly localized natural resources of lithium, as well as the safety issues and the high cost of LIBs, force people to develop rechargeable battery alternatives to LIBs. This has led to intensive research into several new rechargeable battery systems, some of which rely on cations, such as Na^+ (ref. 1 and 2), K^+ (ref. 3), Mg^{2+} (ref. 4 and 5) and Zn^{2+},[6,7] shuttling between cathode and anode electrodes. A bottleneck for the development of these batteries is a limited choice of suitable cathode and anode materials that exhibit satisfactory battery performance.

Two-dimensional (2D) materials such as graphene[8,9] and transition metal dichalcogenides[10–12] have long been studied as potential electrode materials for rechargeable batteries. Besides these materials, 2D transition metal carbides with a general formula of M_nC_{n-1} (MXenes) where $n = 1$–4 and "M" represents an early transition metal such as Ti, V, Nb, and Ta have attracted particular attention in recent years.[13–16] As the synthesis of MXenes is usually performed in aqueous solutions containing fluoride ions, the transition metal atoms on the surface of MXenes are initially terminated with O, OH or F groups. Most MXenes are good electronic conductors which makes these materials promising for electrochemical energy storage. Tang *et al.* studied the Li^+ storage properties of Ti_3C_2 and $Ti_3C_2T_2$ (T = F, OH) by first-principles calculations.[14] The prediction was proved experimentally and $Ti_3C_2T_x$ nanosheets could deliver a Li^+ capacity up to 410 mA h g^{-1} with excellent rate capability.[17] Then, Lukatskaya *et al.* showed that $Ti_3C_2T_x$ could accommodate a variety of cations including Li^+, Na^+, K^+, NH_4^+, Mg^{2+} and Al^{3+}, giving rise to large volumetric capacitance.[18] Xie *et al.* revealed the cation storage mechanisms of MXene monolayers by first-principles calculations,[13] which showed that cation adsorption on MXene monolayers occurs in a relatively low voltage window, suggesting their potential applications as an anode material for rechargeable batteries. In spite of the promising electrochemical properties of MXene monolayers for cation adsorption, their ability to adsorb anions has not been studied.

Compared to the booming growth of metal-ion batteries, rechargeable batteries working with anion storage are underdeveloped. The best-known anion storage species is OH^- [19], which is used in alkaline batteries and nickel-metal hydride batteries. Fluoride ion batteries based on F^- storage[20–23] and recently developed dual-ion batteries, based on intercalation of $TFSI^-$ [24,25] or PF_6^- [24] at the cathode side, offer alternative choices. After fluorine, chlorine is the second most electronegative element and chloride ions (Cl^-) are very stable in a large electrochemical window. It's also the least expensive anion. These features make it possible to develop high voltage

[a]Key Laboratory of Physics and Technology for Advanced Batteries (Ministry of Education), College of Physics, Jilin University, Changchun 130012, China. E-mail: yjwei@jlu.edu.cn; gchen@jlu.edu.cn

[b]Department of Materials Science & Engineering, A. J. Drexel Nanomaterials Institute, Drexel University, Philadelphia, Pennsylvania 19104, USA. E-mail: yg36@drexel.edu

[c]Department of Physics, College of Science, Yanbian University, Yanji 133002, China

† Electronic supplementary information (ESI) available. See DOI: 10.1039/c7ta09057a

chloride ion batteries (CIBs) using suitable Cl^- storage materials. Transition metal chloride salts (MCl_n, such as VCl_3, $BiCl_3$, and $CoCl_2$ (ref. 26 and 27)), oxychloride transition metal salts (MOCl, such as FeOCl,[28–31] BiOCl[28,29] and VOCl[32]) and polypyrrole chloride[33] have been used as the cathode material for CIBs, with a suitable metal (M′ = Li, Mg, or Zn) as the anode. Many of these studies have shown that the experimental capacities of CIBs are much smaller than their theoretical capacities. For example, Zhao *et al.* have shown that $BiCl_2$ exhibits a discharge capacity of 176.6 mA h g^{-1} at a small current density of 3 mA g^{-1} which is 69% of its theoretical capacity of 255 mA h g^{-1} in CIBs. Moreover, the experimental capacity of $CoCl_2$ (105.2 mA h g^{-1}) is only 25% of its theoretical capacity (412.8 mA h g^{-1}).[26] This could be attributed to the large ionic radii of Cl^-, which results in sluggish kinetics for Cl^- diffusion into the host framework. In addition, a large volume change, for example, ~450% for the Co to $CoCl_2$ and Fe to $FeCl_2$ conversion reactions, occurs during charge–discharge cycling. This may break the electric contact between the particles of the active material, and/or cause the active material falling off from the current collector, resulting in a dramatic capacity decay.

On account of these problems, for the first time, a new Cl^- storage mechanism based on Cl^- adsorption on two-dimensional (2D) materials is proposed in this work. First-principles calculations based on density functional theory (DFT) and the partial particle swarm optimization (PPSO) algorithm[34] were used to study the electrochemical properties of Ti_2C monolayers for adsorption of Cl^- anions. The large surface area of MXene monolayers provides many more sites for Cl^- storage than bulk materials. Of more significant interest is that the surface adsorption of Cl^- may require a much lower kinetic barrier comparing to the Cl^- diffusion barrier in bulk materials. Thus, MXene monolayers were expected to show a large reversible Cl^- capacity and high rate capability. Cl was shown to be present on the surface of MXenes in the case of synthesis using LiF and HCl etching solutions.[35] The PPSO algorithm was used in this study to determine the most favorable Cl^- adsorption phase because it effectively searches for the global minima in the energy landscape and avoids the blindness and uncertainty of artificially setting of adsorbed Cl^-. The results predicted a large Cl^- storage capacity and high voltage for Ti_2C monolayers. The low Cl^- diffusion barriers suggested excellent rate capability of this 2D material. Moreover, the effects of terminal groups (T = OH, O, or F) on the Cl^- storage properties of Ti_2C were discussed as well.

2. Computational methods

First-principles calculations were performed in the framework of density functional theory (DFT) implemented in the Vienna ab initio simulation package (VASP).[36] The projector augmented wave (PAW)[37] potential was used with a plane-wave cutoff energy of 600 eV. The exchange correlation energy was described by the generalized gradient approximation (GGA) in the scheme proposed by Perdew–Burke–Ernzerhof (PBE).[38] The pseudopotentials utilized the valence state of $3d^34s^1$ for Ti, $2s^22p^2$ for C, $2s^22p^4$ for O, $1s^1$ for H, $2s^22p^5$ for F, and $3s^23p^5$ for Cl. For geometry optimization, a Brillouin-zone integration was performed using a regular Γ centered 9 × 9 × 1 *k*-mesh and a denser 13 × 13 × 1 mesh for the calculation of the density of states (DOS) within the Monkhorst–Pack scheme.[39] Considering the strong correlation in titanium element, the electronic structure was calculated using a GGA plus Hubbard *U* (GGA + *U*) method.[40] A *U* value of 4.2 eV was used, whose efficacy has been proven for several Ti-based MXenes, such as Ti_3C_2 (ref. 41, 42) and Ti_2N[43]. To avoid interactions between MXene monolayers and their periodically repeated images along the *c* axis, a large vacuum space of 20 Å was used. Geometry optimizations were performed by the conjugated gradient method, and the convergence threshold was set as 1×10^{-6} eV per atom in energy and 0.01 eV $Å^{-1}$ in force.

To simulate the adsorption and diffusion of Cl^- on Ti_2C and Ti_2CT_2 monolayers, a 3 × 3 × 1 supercell containing one adsorbed Cl^- was used. The van der Waals (vdW) force between Cl^- and the MXene monolayer was accurately addressed using a newly developed vdW-inclusive DFT-D3 method,[44] which introduced empirical dispersion corrections implemented by Grimme. In analyzing the Cl^- diffusion behavior on MXene monolayers, the climbing-image nudged elastic band (CI-NEB)[45] method was used. For the diffusion of a single Cl^- ion on MXenes, seven images, including the initial and final positions, were used for CI-NEB calculations. The force convergence criterion for structural optimization was set at 0.01 eV $Å^{-1}$. Before CI-NEB calculations, the initial and final state structures were optimized by DFT.

The structure of Cl^- adsorbed Ti_2C and Ti_2CT_2 monolayers was determined by using the PPSO algorithm using the crystal structure analysis by the particle swarm optimization (CALYPSO) method developed by Ma's group.[46,47] In a 3 × 3 × 1 hexagonal supercell, the coordinates of Ti and C (Ti/C = 2/1, atomic ratio) were fixed, while allowing the coordinates of Cl^- to be searched. The PPSO search lasted for at least 20 generation loops, with 20 different Cl^- adsorption patterns randomly generated in each loop and then relaxed by DFT calculations. Twelve high-energy structures of each iteration loop were discarded and the remaining eight structures were kept in the subsequent PPSO algorithm until the lowest energy was obtained, which meant that the search process converged to an optimal Cl^- adsorption structure.

3. Results and discussion

The structure of the Ti_2C MXene was viewed as a Ti bilayer intercalated by a C layer forming an edge-shared Ti_6C octahedron (Fig. 1a). The hexagonal unit cell contained one C and two Ti atoms, and the optimized lattice constant was $a = b = 3.021$ Å, and the average Ti–C bond length is 2.095 Å, which was consistent with previous results.[48] On the surface of the Ti_2C monolayer, three possible sites were suggested for Cl^- adsorption: on top of a hexagonal center, on top of a C atom, or on top of a Ti atom (sites "a"–"c", respectively). The calculated total DOS showed that Ti_2C was metallic, as indicated by the Fermi levels within the electronic states (Fig. 1b). This offered an intrinsic high electronic conductivity, which might endow Ti_2C with promising electrochemical properties for rechargeable batteries.

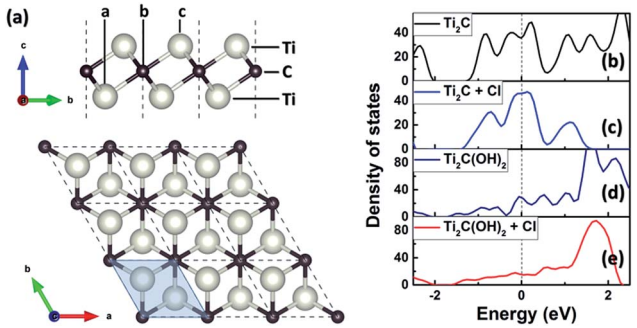

Fig. 1 (a) Side (up) and top (down) views of a Ti_2C monolayer; *a*, *b* and *c* represent the possible adsorption sites for Cl^-. DOS of (b) Ti_2C, (c) Cl-adsorbed Ti_2C, (d) $Ti_2C(OH)_2$, and (e) Cl-adsorbed $Ti_2C(OH)_2$.

3.1 Dilute Cl-adsorption on the Ti_2C monolayer

The adsorption behavior of a single Cl^- ion on the Ti_2C monolayer was examined, with a $3 \times 3 \times 1$ supercell that was sufficiently large to avoid interaction between Cl^- ions. This corresponded to a chemical formula of $Ti_2CCl_{1/9}$. The most favorable adsorption site was identified by adsorption energy calculations using the following equation:

$$E_{ad} = (E_{Ti_2CCl_x} - E_{Ti_2C} - xE_{Cl})/x \quad (1)$$

where E_{ad} is the adsorption energy, $E_{Ti_2CCl_x}$ and E_{Ti_2C} are the total energies of the Ti_2C supercells with and without a Cl^- ion, respectively, E_{Cl} is the energy of Cl in the bulk state, and x the concentration of Cl^- per Ti_2C formula, which was 1/9 for single Cl^- adsorption. Two distinct adsorption sites, "*a*" and "*b*", were identified by the PPSO algorithm (Fig. 2a and b, respectively). For comparison, site "*c*", with a smaller adsorption energy (−2.974 eV), was also taken into account (Fig. 2c). For a single Cl^- ion, "*a*" site (−3.985 eV) exhibited a smaller E_{ad} than the other sites, while "*b*" site (−3.807 eV) took the second favored place, with a slightly larger E_{ad}. This might have been due to the adsorbed Cl^- being triply coordinated with Ti, for both "*a*" and "*b*" sites. Overall, adsorption on the top of the hexagonal center, *i.e.*, site "*a*", was more favorable than the other positions. The E_{ad} at site "*a*", without considering vdW, was −3.879 eV, which was 0.106 eV higher than that of −3.985 eV calculated with the vdW-inclusive DFT-D3 method. This indicated that the vdW contribution to the total bonding energy was only 2.66 % and, thus, the adsorbed Cl^- ion formed a strong chemical bond with the Ti_2C monolayer.

Greater insight into the Cl^- adsorption process was obtained by evaluating the charge density difference between the Ti_2C supercells with and without Cl^- ions at the "*a*", "*b*", and "*c*" sites (Fig. 2d–f). The density isosurface was defined as

$$\Delta\rho = \rho_{Ti_2C+Cl} - \rho_{Ti_2C} - \rho_{Cl} \quad (2)$$

Electron-rich regions were noticed around Cl, while an electron-deficient region appeared between Cl and Ti_2C, suggesting an ionic character in the Ti_2C–Cl bonding. For all three adsorption configurations, the adsorbed Cl accepted electrons from Ti_2C and, to be more exact, accepted mainly from coordinated Ti atoms. It was speculated that the number of

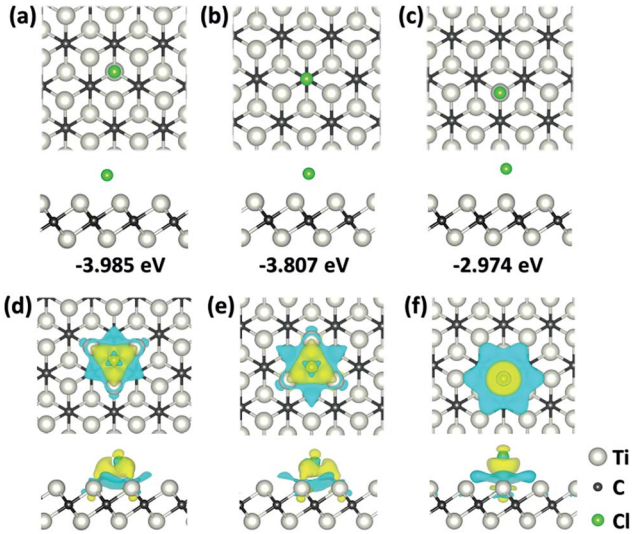

Fig. 2 (a)–(c) Configurations and adsorption energies of single Cl^- (green balls) adsorbed onto Ti_2C monolayers. (d)–(f) Charge density difference isosurfaces of single Cl^- adsorbed Ti_2C monolayers. Isosurface level set to 0.0025 e $Å^{-3}$; electron-rich regions, yellow; and electron-deficient regions, blue.

transferred electrons at site "*a*" was more than that of sites "*b*" and "*c*". This was quantified by performing Bader charge analysis and the results indicated that the Cl^- ions obtained 0.716, 0.708, and 0.642 e^- per atom, respectively, from the Ti_2C monolayer, which indicated that the Cl^- ions were chemically bonded to the Ti_2C monolayer. It was noted that the degree of ionization at site "*a*" was higher than that of other sites, indicating a stronger bonding of Cl to the Ti_2C monolayer, which agreed with the E_{ad} calculation results.

The rate capability of electrode materials, determined by the kinetic properties of both electron transport and ion diffusion, is one of the most important parameters for battery performance. Here, DOS analysis showed that the Ti_2C monolayer still showed metallic behavior after Cl^- adsorption (Fig. 1c). This ensured fast electron transport in the electrode during the whole Cl^- adsorption/desorption process, which is essential for the high rate capability of the Ti_2C monolayer for CIBs. Moreover, the diffusion properties of Cl^- on the Ti_2C monolayer were examined by CI-NEB analysis. Based on the above analysis, "*a*" was the most favorable site for Cl^- adsorption. Thus, three possible diffusion pathways were predesigned between two neighboring "*a*" sites (Fig. 3a). For path 1, Cl^- moved from one "*a*" site to the nearest "*a*′" site across a "*c*" site, *i.e.*, $a \rightarrow c \rightarrow a'$; for path 2, Cl^- moved from one "*a*" site to the nearest "*a*′" site across a "*b*" site, *i.e.*, $a \rightarrow b \rightarrow a'$; and for path 3, Cl^- moved directly to the nearest neighboring "*a*′" site, *i.e.*, $a \rightarrow a'$. The diffusion barrier profiles for the three pathways showed that path 1 exhibited the largest diffusion barrier, with only one saddle point on top of Ti (Fig. 3b). This was ascribed to the strong coulombic interactions between Cl and Ti because of the short Ti–Cl distance. In comparison, the energy barrier along path 2 was significantly reduced. A local energy minimum was observed at intermediate site "*b*" and two saddle points were

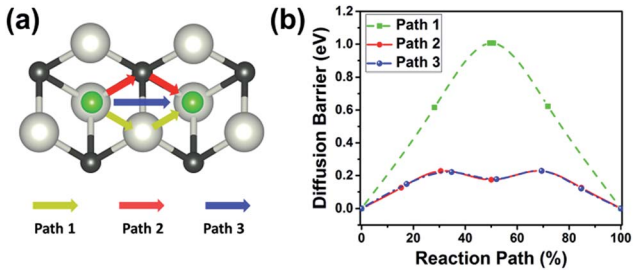

Fig. 3 (a) Possible Cl^- diffusion pathways on a Ti_2C monolayer. (b) Diffusion barrier profiles of Cl^- on a Ti_2C monolayer.

observed in the middle of the a–b and b–a' bridges. The calculated diffusion barrier along path 2 was 0.227 eV, very close to those of Li adsorption on some 2D monolayers, such as 0.25 eV for MoS_2 (ref. 49) and 0.21 eV for VS_2.[50] The barrier was even much smaller than those of Li diffusion on other 2D energy storage materials, such as 0.780 eV for MoN_2 (ref. 51) and 0.330 eV for graphene,[52] suggesting good rate capability of Ti_2C for CIB applications. Path 3 was noted to show a very similar diffusion barrier profile to that of path 2, which indicated that Cl^- did not follow the predesigned linear $a \rightarrow a'$ pathway and, instead, behaved similarly to that in the optimized path 2, as reported for Li^+ diffusion on Ti_3C_2 and Ti_2N monolayers.[14,43] The calculated low diffusion barriers suggest that Ti_2C monolayers can show excellent rate capability in CIB applications.

3.2 High degree Cl adsorption on the Ti_2C monolayer

The PPSO algorithm was applied to examine the adsorption configuration of Ti_2CCl_x at higher adsorption degrees ($x > 1/9$).

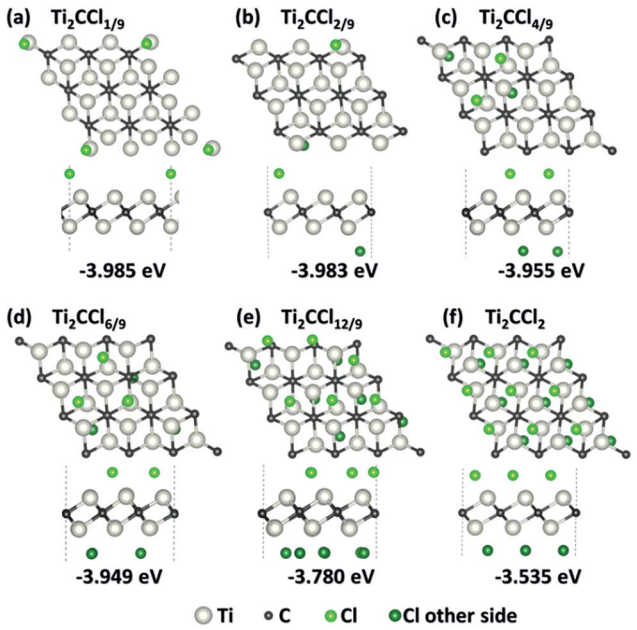

Fig. 4 Optimized configurations and adsorption energies of Ti_2CCl_x monolayers at different adsorption degrees: x = 1/9, 2/9, 4/9, 6/9, 12/9, and 18/9 (a–f, respectively).

The E_{ad} of Ti_2CCl_x was also calculated using eqn (2). The most stable adsorption phase at each Cl^- concentration (x = 2/9, 4/9, 2/3, 4/3, and 2.0) was selected from 400 randomly generated Ti_2CCl_x phases. The optimized adsorption phases and their adsorption energies showed that, when the adsorption degree (x) was ≤4/9, all the adsorbed Cl^- ions were located at the "a" site (Fig. 4a–f). When the adsorption degree increased to $x = 2/3$ and 4/3, additional Cl^- appeared at site "b", and thus both "a" and "b" sites of the Ti_2C monolayer were occupied by Cl^-. When the adsorption degree increased to 2.0, the "b" site was no longer occupied; instead, all the Cl^- ions were located at site "a". This indicated the rearrangement of Cl^-, resulting in highly ordered Cl occupation of "a" sites. Moreover, the calculated E_{ad} became less negative with increased Cl^- concentration, which was attributed to increased repulsion between Cl^- ions. The original layered structure of Ti_2C remained almost unchanged even at a high Cl^- concentration of $x = 2.0$ in Ti_2CCl_x, indicating good structural stability of the Ti_2C monolayer.

To explore the most thermodynamically stable Cl^- adsorption phase, the formation energy of Ti_2CCl_x was calculated with different Cl^- adsorption degrees using the following equation:

$$\Delta E = E_{Ti_2CCl_x} - \frac{x}{2}E_{Ti_2CCl_2} - \left(1 - \frac{x}{2}\right)E_{Ti_2C}, \quad (3)$$

where $E_{Ti_2CCl_x}$, $E_{Ti_2CCl_2}$, and E_{Ti_2C} are the energies of Ti_2CCl_x, Ti_2CCl_2, and Ti_2C, respectively. The calculated ΔE was plotted as a function of adsorption degree x (Fig. 5a). The graphed lines connect the minimum energy structures and end members, Ti_2C and Ti_2CCl_2, to create a convex hull, in which the red points represent phases in the thermodynamic equilibrium and the blue points show unstable phases, consistent with the PPSO algorithm results. The minimum of the convex hull corresponds to the maximum adsorption degree, which was 4/3 for the Ti_2C

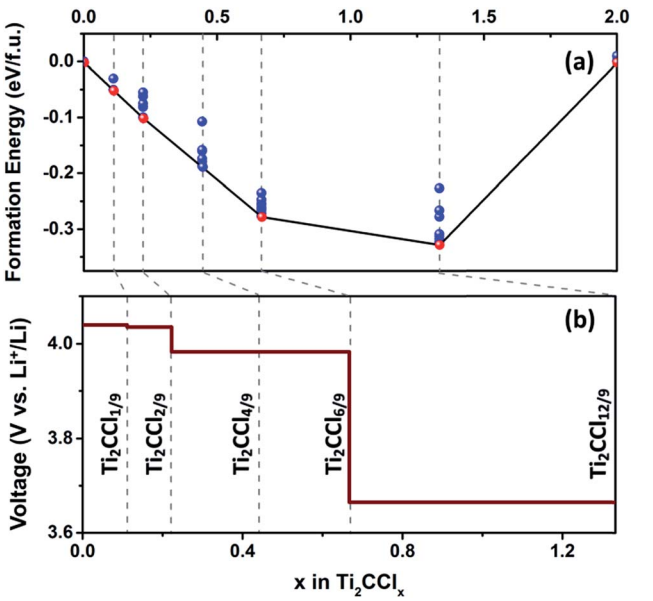

Fig. 5 (a) Convex hull of formation energy (ΔE) *vs.* Cl^- concentration (x) for the Ti_2CCl_x monolayer. (b) Predicted discharge profile of the Ti_2C monolayer for Cl^- adsorption.

monolayer. Compared to the traditional criteria using adsorption energy to estimate the adsorption capacity, the convex hull method offers a more natural and unambiguous tool for capacity estimation. At that point, we need to note that bare MXenes have not yet been produced, even though thermal desorption of O and F species from $Ti_3C_2T_x$ was observed in a vacuum or inert environment.[53] Chlorine can be used to replace those terminations and produce chlorinated Ti_2C. However, as this structure still remains hypothetical, it is important to study Cl^- adsorption on the currently available MXene surfaces. A detailed discussion of Cl^- adsorption capacities on terminated MXenes is presented in the following section.

3.3 Cl^- adsorption on terminated Ti_2CT_2 (T = O, F, and OH) monolayers

As the synthesis of MXenes is usually performed in aqueous solutions containing fluoride ions, the transition metal atoms on the monolayer surfaces are initially terminated with O, F, and OH groups. Theoretical and experimental studies on Li-ion batteries have shown that terminal groups have significant effects on the electrochemical properties of MXenes. Thus, in this section, Cl^- adsorption onto Ti_2CT_2 monolayers with saturated functional groups, including O, F, and OH, was taken into account. The analysis of DOS showed that the Ti_2CF_2 and $Ti_2C(OH)_2$ monolayers retained metallic properties while semiconductor properties were observed for Ti_2CO_2 (Fig. S1, ESI†), which was in good agreement with the previously reported results.[54] DFT calculations showed that these terminal groups preferred to locate at site "*a*" (Fig. S2, ESI†). Therefore, this Ti_2CT_2 configuration was considered in the following calculations. The case of a single Cl^- adsorption on Ti_2CT_2 was first investigated using a $3 \times 3 \times 1$ supercell. The fully relaxed geometries of Cl^- adsorbed on Ti_2CT_2 are shown in Fig. S3 (ESI†). Cl^- adsorption on saturated Ti_2CO_2 and Ti_2CF_2 monolayers produced positive E_{ad}, regardless of the site, "*a*" or "*b*" or "*c*" (Fig. 6). This indicated that Cl^- was not adsorbed onto the O and F terminated Ti_2C monolayers. However, once an O or F vacancy was generated on Ti_2CO_2 and Ti_2CF_2 monolayers, Cl^- migrated to the vicinity of the vacant site with a negative E_{ad}, being −2.685 eV for $Ti_2CO_{17/9}$ and −3.481 eV for $Ti_2CF_{17/9}$. This suggested that unsaturated Ti_2CO_x and Ti_2CF_x monolayers allowed stable Cl^- absorption. In this case, the Cl^- storage capacity depended on the concentration of O and F vacancies. Unlike Ti_2CO_2 and Ti_2CF_2, Cl^- adsorption produced negative E_{ad} on a $Ti_2C(OH)_2$ monolayer at all three possible sites, among which the site "*b*" gave the smallest E_{ad}. Moreover, Cl^- adsorption at OH vacancies was also allowed, judged by the negative E_{ad} for $Ti_2C(OH)_{17/9}$.

The diverse Cl^- adsorption behavior on Ti_2C and Ti_2CT_2 monolayers was analyzed by using electron localization functions (ELFs), which referred to the jellium-like homogeneous electron gas and renormalized the value to 0.00–1.00. Values of 1.00 and 0.50 corresponded to fully localized and delocalized electrons, respectively, while 0.00 referred to a very low charge density. The ELF of the (110) slice of Ti_2C and Ti_2CT_2

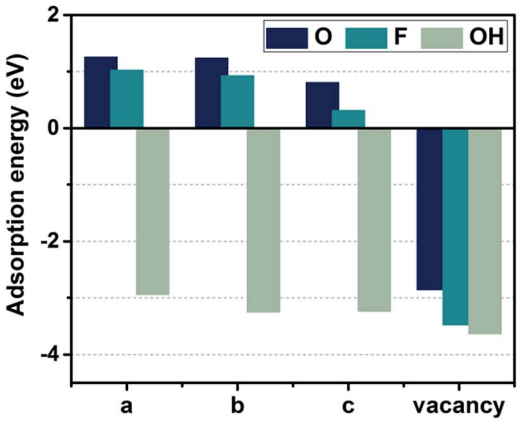

Fig. 6 Adsorption energies of Cl^- onto Ti_2CO_2, Ti_2CF_2, and $Ti_2C(OH)_2$ monolayers at *a*, *b*, and *c* sites, respectively. "Vacancy" corresponds to the adsorption energies of Ti_2CT_2 (T = O, F, and OH) monolayers with one "T" vacancy.

monolayers showed a cloud of lone-pair electrons distributed on the surface of Ti_2C and $Ti_2C(OH)_2$, which provided effective bonding electrons for Cl^- (Fig. 7). For Ti_2CO_2 and Ti_2CF_2, the original lone-pair electrons were localized around the O and F terminals, thus making it difficult to form ionic bonds with Cl^-.

The structures of $Ti_2C(OH)_2Cl_x$ monolayers with high Cl^- degrees of x = 1/9, 2/9, 4/9, 2/3, 4/3, and 2 were examined by applying the PPSO algorithm. The optimized adsorption phases and their adsorption energies showed that the calculated E_{ad} became less negative with increasing adsorption degree, because of the repulsion between Cl^- ions (Fig. 8). For single Cl^- adsorption, site "*b*" was more favorable than other sites. Bader charge analysis showed that Cl^- obtained 0.761 e^- per atom from the $Ti_2C(OH)_2$ monolayer, indicating ionic bonding of Cl^- with the monolayer. DOS analysis showed that both $Ti_2C(OH)_2$ and $Ti_2C(OH)_2Cl_x$ exhibited metallic properties (Fig. 1d and e, respectively), ensuring good electrical conductivity of the material during Cl^- adsorption/desorption. In addition, the minimum diffusion barrier of Cl^- on $Ti_2C(OH)_2$

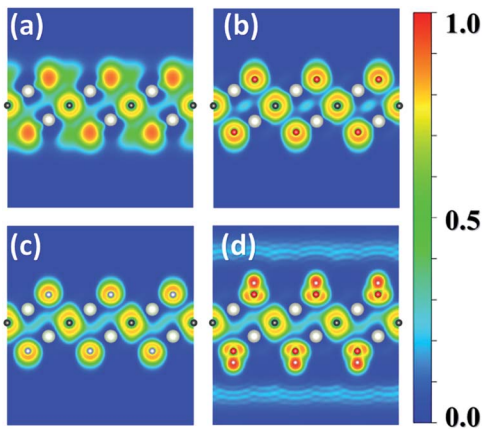

Fig. 7 Electron localization function isosurfaces of Ti_2C (a), Ti_2CO_2 (b), Ti_2CF_2 (c) and $Ti_2C(OH)_2$ (d) monolayers.

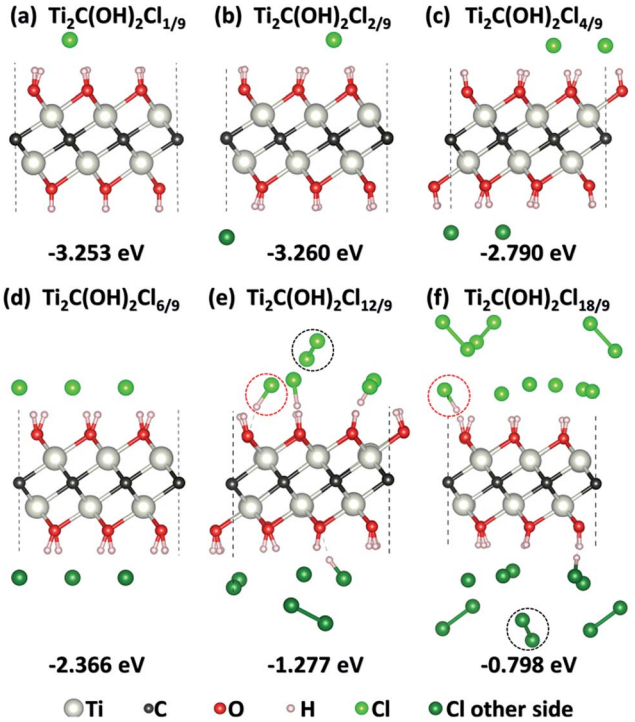

Fig. 8 Optimized structures and adsorption energies of $Ti_2C(OH)_2Cl_x$ monolayers at different adsorption degrees: $x = 1/9$, 2/9, 4/9, 6/9, 12/9, and 18/9, (a)–(f), respectively.

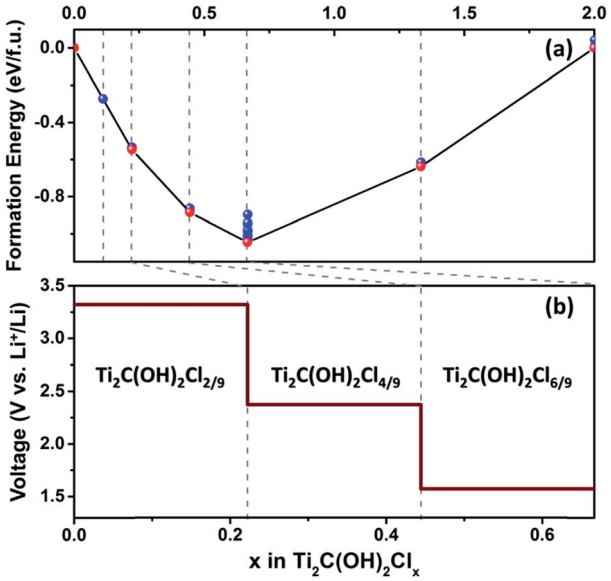

Fig. 9 (a) Convex hull of formation energy (ΔE) *vs.* Cl^- concentration (x) for $Ti_2C(OH)_2Cl_x$ monolayers. (b) Predicted discharge profile of the $Ti_2C(OH)_2$ monolayer for Cl^- adsorption.

was calculated to be 0.057 eV along the $b \rightarrow c \rightarrow b'$ path (Fig. S4, ESI†). And in the range of compositions $1/9 \leq x \leq 2/3$, Cl adsorption sites were the arrangement and combination of site "*a*" on the $Ti_2C(OH)_2$ monolayer. However, the monolayer surface chemistry became more complex at higher Cl^- degrees ($x = 4/3$ and 2). For these cases, some Cl^- formed an H–Cl bond with the surface OH group; meanwhile other Cl^- formed Cl–Cl bonds. This indicated that HCl and Cl_2 would be formed during deep Cl^- adsorption, and this could cause rapid capacity fading and serious corrosion of cell components. Moreover, the convex hull profile of ΔE *versus* x demonstrated that $Ti_2C(OH)_2Cl_{2/3}$ was the most thermodynamically stable Cl^- adsorption phase (Fig. 9a).

3.4 Theoretical capacity and working potential

The specific capacity and working voltage of the cathode material determine the energy density of rechargeable batteries. Assuming that Li metal is used as the anode material of a CIB cell, the open circuit voltage of Ti_2C and $Ti_2C(OH)_2$ monolayers at different Cl^- adsorption degrees was calculated using the following equation:

$$V = -\frac{\left[E_{Ti_2CCl_x[Ti_2C(OH)_2Cl_x]} - E_{Ti_2C[Ti_2C(OH)_2]} - x\left(\mu_{Cl} + \Delta\mu_{Cl/Li}\right)\right]}{xne}, \quad (4)$$

where $E_{Ti_2CCl_x[Ti_2C(OH)_2Cl_x]}$ and $E_{Ti_2C[Ti_2C(OH)_2]}$ are the total energies of Ti_2C and $Ti_2C(OH)_2$ with and without Cl ions, respectively, μ_{Cl} is the chemical potential of Cl, $\Delta\mu_{Cl/Li}$ is the difference in chemical potentials between Cl and Li, and n is the valence state of fully ionized Cl, *i.e.*, $n = 1.0$. The calculated discharge profiles of Ti_2C and $Ti_2C(OH)_2$ monolayers are displayed in Fig. 5b and 9b, respectively. Note that the maximum Cl^- adsorption degree was set at the minimum point of the convex hull, according to the above discussion. Calculations showed that the Ti_2C monolayer exhibited several voltage plateaus in the 4.0–3.5 V voltage window, suggesting that it could serve as a high voltage cathode material for CIBs. In comparison, the voltage plateaus of $Ti_2C(OH)_2$ monolayers decreased to 3.5–1.5 V, indicating that terminal OH groups decreased Ti_2C's working voltage. Finally, the maximum Cl^- capacities of Ti_2C and $Ti_2C(OH)_2$ monolayers were calculated from

$$C_A = xnF/M_{Ti_2C[Ti_2C(OH)_2]} \quad (5)$$

where x is the maximum Cl^- adsorption degree determined from the convex hull, n is the valence state of fully ionized Cl, F is the Faraday constant (26 801 mA h mol^{-1}), and $M_{Ti_2C[Ti_2C(OH)_2]}$ is the molar weight of Ti_2C or $Ti_2C(OH)_2$. Based on these calculations, a theoretical Cl^- capacity of 331 mA h g^{-1} was predicted for single-layer Ti_2C and 126 mA h g^{-1} for single-layer $Ti_2C(OH)_2$. Compared to $Ti_2C(OH)_2$, the bare Ti_2C without terminal groups showed a larger capacity and a higher working voltage. This resulted in a theoretical specific energy of 1269 W h kg^{-1} at the material level. We also expect that the Ti_3C_2 MXene will show a similar trend. This computational study is a first step towards the exploration of MXenes for CIBs, but it is also important for understanding the performance of titanium carbide MXenes in capacitive deionisation or membrane desalination, where NaCl-rich solutions are handled.

4. Conclusions

In summary, the electrochemical properties of Ti_2C monolayers for Cl^- adsorption were investigated on the basis of first-principles calculations combined with the PPSO algorithm. The results showed that Cl^- was stably absorbed on the Ti_2C monolayer. The metallic character of Ti_2C during the whole Cl^- adsorption/desorption process ensured high electronic conductivity of the electrode. The most energetically favorable Cl^- diffusion pathway was identified, with a low diffusion barrier of 0.22 eV that gave rise to an excellent rate capability. The PPSO algorithm showed that the maximum Cl^- adsorption degree (x) on the Ti_2C monolayer was $x = 4/3$, resulting in a theoretical capacity of 331 mA h g^{-1}. The discharge profile of the Ti_2C monolayer was composed of several voltage plateaus in the voltage window of 4.0–3.5 V, indicating that this 2D MXene could be used as a cathode material for CIBs. The effects of terminal groups on the Cl^- storage properties of Ti_2C were examined as well. Cl^- was found not to be adsorbed on O and F-terminated Ti_2C layers. However, once O or F vacancies were generated on a monolayer, Cl^- could be adsorbed at the vicinity of the vacant sites. Unlike Ti_2CO_2 and Ti_2CF_2, $Ti_2C(OH)_2$ monolayers can adsorb Cl^-. However, the corresponding capacity of 126 mA h g^{-1} was smaller than that of Ti_2C monolayers. Moreover, the working voltage of $Ti_2C(OH)_2$ was decreased by OH terminal groups.

Conflicts of interest

There are no conflicts to declare.

Acknowledgements

This work was supported by the Ministry of Science and Technology of China (No. 2015CB251103), the National Natural Science Foundation of China (Nos. 51472104 and 21473075), the One Thousand Talents Recruitment Program of Foreign Experts (Prof. Yury Gogotsi), and the Graduate Innovation Fund of Jilin University (No. 2017006). Theoretical calculations were carried out at the Tianjin National Supercomputer Centre.

References

1 V. Palomares, P. Serras, I. Villaluenga, K. B. Hueso, J. Carretero-González and T. Rojo, *Energy Environ. Sci.*, 2012, **5**, 5884.
2 H. Pan, Y.-S. Hu and L. Chen, *Energy Environ. Sci.*, 2013, **6**, 2338.
3 A. Eftekhari, *J. Power Sources*, 2004, **126**, 221–228.
4 R. Mohtadi and F. Mizuno, *Beilstein J. Nanotechnol.*, 2014, **5**, 1291–1311.
5 H. D. Yoo, I. Shterenberg, Y. Gofer, G. Gershinsky, N. Pour and D. Aurbach, *Energy Environ. Sci.*, 2013, **6**, 2265.
6 C. Xu, B. Li, H. Du and F. Kang, *Angew. Chem., Int. Ed.*, 2012, **51**, 933–935.
7 L. Zhang, L. Chen, X. Zhou and Z. Liu, *Adv. Energy Mater.*, 2015, **5**, 1400930.
8 K. S. Novoselov, V. I. Fal′ko, L. Colombo, P. R. Gellert, M. G. Schwab and K. Kim, *Nature*, 2012, **490**, 192–200.
9 Y. Jing, Z. Zhou, C. R. Cabrera and Z. Chen, *J. Mater. Chem. A*, 2014, **2**, 12104.
10 Y. Li, D. Wu, Z. Zhou, C. R. Cabrera and Z. Chen, *J. Phys. Chem. Lett.*, 2012, **3**, 2221–2227.
11 D. B. Putungan, S.-H. Lin and J.-L. Kuo, *ACS Appl. Mater. Interfaces*, 2016, **8**, 18754–18762.
12 Q. Tang, Z. Zhou and Z. Chen, *Wiley Interdiscip. Rev.: Comput. Mol. Sci.*, 2015, **5**, 360–379.
13 Y. Xie, Y. Dall'Agnese, M. Naguib, Y. Gogotsi, M. W. Barsoum, H. L. Zhuang and P. R. C. Kent, *ACS Nano*, 2014, **8**, 9606–9615.
14 Q. Tang, Z. Zhou and P. Shen, *J. Am. Chem. Soc.*, 2012, **134**, 16909–16916.
15 D. Sun, Q. Hu, J. Chen, X. Zhang, L. Wang, Q. Wu and A. Zhou, *ACS Appl. Mater. Interfaces*, 2016, **8**, 74–81.
16 T. Yu, S. Zhang, F. Li, Z. Zhao, L. Liu, H. Xu and G. Yang, *J Mater Chem A*, 2017, **5**, 18698–18706.
17 O. Mashtalir, M. Naguib, V. N. Mochalin, Y. Dall'Agnese, M. Heon, M. W. Barsoum and Y. Gogotsi, *Nat. Commun.*, 2013, **4**, 1716.
18 M. R. Lukatskaya, O. Mashtalir, C. E. Ren, Y. Dall'Agnese, P. Rozier, P. L. Taberna, M. Naguib, P. Simon, M. W. Barsoum and Y. Gogotsi, *Science*, 2013, **341**, 1502–1505.
19 R. Shivkumar, G. Paruthimal Kalaignan and T. Vasudevan, *J. Power Sources*, 1998, **75**, 90–100.
20 F. Gschwind, G. Rodriguez-Garcia, D. J. S. Sandbeck, A. Gross, M. Weil, M. Fichtner and N. Hörmann, *J. Fluorine Chem.*, 2016, **182**, 76–90.
21 M. Anji Reddy and M. Fichtner, *J. Mater. Chem.*, 2011, **21**, 17059.
22 C. Rongeat, M. Anji Reddy, T. Diemant, R. J. Behm and M. Fichtner, *J Mater Chem A*, 2014, **2**, 20861–20872.
23 M. A. Nowroozi, K. Wissel, J. Rohrer, A. R. Munnangi and O. Clemens, *Chem. Mater.*, 2017, **29**, 3441–3453.
24 X. Qi, B. Blizanac, A. DuPasquier, P. Meister, T. Placke, M. Oljaca, J. Li and M. Winter, *Phys. Chem. Chem. Phys.*, 2014, **16**, 25306–25313.
25 K. Beltrop, P. Meister, S. Klein, A. Heckmann, M. Grünebaum, H.-D. Wiemhöfer, M. Winter and T. Placke, *Electrochim. Acta*, 2016, **209**, 44–55.
26 X. Zhao, S. Ren, M. Bruns and M. Fichtner, *J. Power Sources*, 2014, **245**, 706–711.
27 F. Gschwind, D. Steinle, D. Sandbeck, C. Schmidt and E. von Hauff, *ChemistryOpen*, 2016, **5**, 525–530.
28 X. Zhao, Q. Li, Z. Zhao-Karger, P. Gao, K. Fink, X. Shen and M. Fichtner, *ACS Appl. Mater. Interfaces*, 2014, **6**, 10997–11000.
29 X. Zhao, Z. Zhao-Karger, D. Wang and M. Fichtner, *Angew. Chem., Int. Ed.*, 2013, **52**, 13621–13624.
30 T. Yu, Q. Li, X. Zhao, H. Xia, L. Ma, J. Wang, Y. S. Meng and X. Shen, *ACS Energy Lett.*, 2017, **2**, 2341–2348.
31 X. Zhao, Q. Li, T. Yu, M. Yang, K. Fink and X. Shen, *Sci. Rep.*, 2016, **6**, 19448.

32 P. Gao, M. A. Reddy, X. Mu, T. Diemant, L. Zhang, Z. Zhao-Karger, V. S. K. Chakravadhanula, O. Clemens, R. J. Behm and M. Fichtner, *Angew. Chem., Int. Ed.*, 2016, **55**, 4285–4290.
33 X. Zhao, Z. Zhao, M. Yang, H. Xia, T. Yu and X. Shen, *ACS Appl. Mater. Interfaces*, 2017, **9**, 2535–2540.
34 B. Gao, X. Shao, J. Lv, Y. Wang and Y. Ma, *J. Phys. Chem. C*, 2015, **119**, 20111–20118.
35 M. Alhabeb, K. Maleski, B. Anasori, P. Lelyukh, L. Clark, S. Sin and Y. Gogotsi, *Chem. Mater.*, 2017, **29**, 7633–7644.
36 G. Kresse and J. Furthmüller, *Phys. Rev. B*, 1996, **54**, 11169–11186.
37 G. Kresse and D. Joubert, *Phys. Rev. B*, 1999, **59**, 1758–1775.
38 J. P. Perdew, K. Burke and M. Ernzerhof, *Phys. Rev. Lett.*, 1996, **77**, 3865–3868.
39 H. J. Monkhorst and J. D. Pack, *Phys. Rev. B*, 1976, **13**, 5188–5192.
40 V. I. Anisimov, I. V. Solovyev, M. A. Korotin, M. T. Czyżyk and G. A. Sawatzky, *Phys. Rev. B*, 1993, **48**, 16929–16934.
41 S. Kajiyama, L. Szabova, K. Sodeyama, H. Iinuma, R. Morita, K. Gotoh, Y. Tateyama, M. Okubo and A. Yamada, *ACS Nano*, 2016, **10**, 3334–3341.
42 B. Anasori, Y. Xie, M. Beidaghi, J. Lu, B. C. Hosler, L. Hultman, P. R. C. Kent, Y. Gogotsi and M. W. Barsoum, *ACS Nano*, 2015, **9**, 9507–9516.
43 D. Wang, Y. Gao, Y. Liu, D. Jin, Y. Gogotsi, X. Meng, F. Du, G. Chen and Y. Wei, *J. Phys. Chem. C*, 2017, **121**, 13025–13034.
44 S. Grimme, J. Antony, S. Ehrlich and H. Krieg, *J. Chem. Phys.*, 2010, **132**, 154104.
45 G. Henkelman, B. P. Uberuaga and H. Jónsson, *J. Chem. Phys.*, 2000, **113**, 9901–9904.
46 Y. Wang, J. Lv, L. Zhu and Y. Ma, *Phys. Rev. B*, 2010, **82**, 094116.
47 Y. Wang, J. Lv, L. Zhu and Y. Ma, *Comput. Phys. Commun.*, 2012, **183**, 2063–2070.
48 S. Zhao, W. Kang and J. Xue, *J. Phys. Chem. C*, 2014, **118**, 14983–14990.
49 Y. Jing, Z. Zhou, C. R. Cabrera and Z. Chen, *J. Phys. Chem. C*, 2013, **117**, 25409–25413.
50 D. Wang, Y. Liu, X. Meng, Y. Wei, Y. Zhao, Q. Pang and G. Chen, *J Mater Chem A*, 2017, **5**, 21370–21377.
51 X. Zhang, Z. Yu, S.-S. Wang, S. Guan, H. Y. Yang, Y. Yao and S. A. Yang, *J Mater Chem A*, 2016, **4**, 15224–15231.
52 C. Uthaisar and V. Barone, *Nano Lett.*, 2010, **10**, 2838–2842.
53 O. Mashtalir, M. R. Lukatskaya, A. I. Kolesnikov, E. Raymundo-Piñero, M. Naguib, M. W. Barsoum and Y. Gogotsi, *Nanoscale*, 2016, **8**, 9128–9133.
54 S. Kajiyama, L. Szabova, H. Iinuma, A. Sugahara, K. Gotoh, K. Sodeyama, Y. Tateyama, M. Okubo and A. Yamada, *Adv. Energy Mater.*, 2017, **7**, 1601873.